Holzforschung, Vol. 65, pp. 377–387, 2011 • Copyright © by Walter de Gruyter • Berlin • New York. DOI 10.1515/HF.2011.050

Air-coupled ultrasound inspection of glued laminated timber

Sergio J. Sanabria[1,*], Roman Furrer[1], Jürg Neuenschwander[1], Peter Niemz[2] and Urs Sennhauser[1]

[1] Electronics/Metrology/Reliability Laboratory, Empa, Swiss Federal Laboratories for Materials Science and Technology, Düebendorf, Switzerland

[2] Laboratory for Wood Physics and Non-Destructive Testing Methods, Institute for Building Materials, ETH Zurich, Zurich, Switzerland

*Corresponding author.
Electronics/Metrology/Reliability Laboratory, Empa, Swiss Federal Laboratories for Materials Science and Technology, Überlandstrasse 129, CH-8600 Düebendorf, Switzerland
E-mail: sergio.sanabria@empa.ch

Abstract

A novel air-coupled ultrasound (ACU) 120 kHz normal transmission system enabled successful imaging of bonding and saw cut defects in multilayered glulam beams up to 280 mm in height with a signal-to-noise ratio (SNR) of 40 dB. The main wave propagation paths were modeled; quasi-longitudinal and quasi-transverse modes were coupled in each lamella and the sound field was found to be shifted from the insonification axis as a function of the ring angle, leading to interference of wave paths in the receiver and to 15 dB amplitude variability in defect-free glulam. The assessment was improved with spatial processing algorithms that profited from the arbitrary scanning resolution and high reproducibility of ACU. Overlapped averaging reduced in-band noise by 15 dB, amplitude tracking captured only the first incoming oscillation, thus minimizing diffraction around defect regions, and image normalization compensated 6 dB of systematic amplitude variability across the fiber direction. The application of ACU to *in situ* defect monitoring was demonstrated by using multiparameter difference imaging of measurements of the same sample with and without saw cut defects. The segmentation of the defect geometry was improved significantly and the amplitude variability was reduced by 10 dB. Further work is planned to model additional insonification setups and grain and density heterogeneities.

Keywords: air-coupled ultrasound; amplitude tracking; bonding quality; delamination; energy flux shift; glued laminated timber; *in situ* flaw monitoring; multiparameter difference imaging; non-contact ultrasonics; non-destructive evaluation; saw cut defect; spatial signal processing; ultrasound wave propagation; wood heterogeneity.

Introduction

A reliable bonding quality assessment of glued laminated timber (glulam) is necessary to reduce security hazards and maximize the life span of wooden constructions (Bucur 2010). During fabrication, inadequate environmental, pressing, and curing parameters can lead to glue line defects (Dunky and Niemz 2002). The choice of the gluing products must take into account the final climatic conditions of the building, as for instance urea resins can be hydrolytically removed and polyurethane based products need a minimum moisture level during and after the gluing (Kägi et al. 2006; Schrödter and Niemz 2006). During utilization, the duration of load effect (DOL) can reduce the strength of glued timber products (Gustafsson et al. 1998; Dill-Langer 2004). Stresses in glulam induced by in-service moisture and climate variation, which may lead to cracks and delaminations, is a matter of intensive investigation (Jönsson 2004; Jönsson and Svensson 2004; Jönsson 2005; Scheffler et al. 2007; Niemz and Gereke 2009; Angst and Malo 2010; Follrich et al. 2010). Therefore, a periodical integrity test of the glue lines is required during the full life cycle of a glulam structural member.

Current European standards define destructive tests on random samples of the total production (EN 391 2001; EN 14080 2005). Non-destructive evaluation (NDE) methods enable *in situ* diagnoses of flaws developed during utilization. Infrared thermography is limited to inspection of thin veneer (Berglind and Dillenz 2003). Computed tomography (CT) methods based on non-refracting radiation (X-ray, neutrons) can detect the absence of adhesive in wood composites (Hu and Gagnon 2007; Osterloh et al. 2008; Sanabria et al. 2010a). However, the hazardous nature of these methods still constrains their application on site. Ultrasonics are easily portable and are sensitive to delaminated interfaces due to the quasi-specular wave reflection at air/solid interfaces (Maeva et al. 2004). In the case of wood, the coupling of energy between transducers and sample is problematic, since agents such as gel, grease, or liquid may penetrate the latter. Therefore, dry contact is preferred for glulam inspection (Dimanche et al. 1994; Dill-Langer et al. 2005a,b). The reproducibility is limited by the adjustment of the coupling pressure at each insonified position. Ultrasonic imaging based on continuous transducer scanning is generally not possible.

Air-coupled ultrasonics (ACU) overcomes these drawbacks; however, the coupling of $<0.5\%$ of transmitted energy into solids has traditionally limited its applicability to thin samples. Recent developments in transducer technologies (Kunkle et al. 2006) and dedicated low-noise electronics are the cornerstones to NDE of thick structural members (Alger-

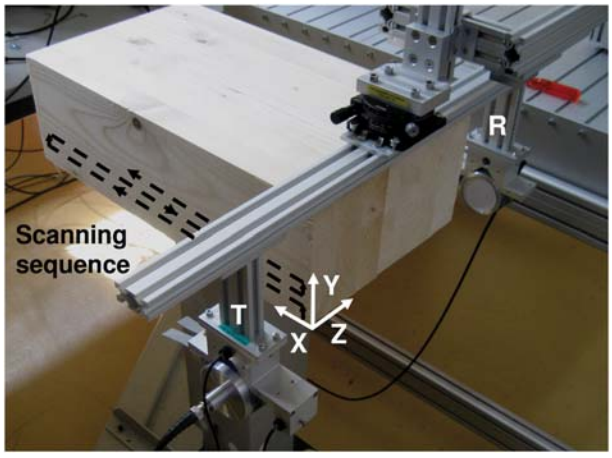

Figure 1 Air-coupled ultrasound (ACU) normal transmission setup (NTM). T and R are 120 kHz transmitter and receiver transducers, respectively, with an active diameter of 50 mm.

non et al. 2008). ACU has previously been used to assess solid wood boards, particleboard, fiber composites, veneer and glued timber boards (Fagus GreCon Greten GmbH & Co. KG 1994; Blum 1997; Benedetti 2003; Stöessel 2004; Gan et al. 2005; Hasenstab 2006; Hyvärinen 2007; Vun et al. 2008; Blomme et al. 2010; Dahmen et al. 2010; Hsu et al. 2010; Sanabria et al. 2010b). To the best of our knowledge, there is no current ACU application for the inspection of glulam.

In this work, a novel ACU normal transmission mode (NTM) setup and signal processing algorithms were developed and applied to the imaging of bonding defects in multilayered glulam beams. The main propagation paths and the impact of wood anisotropy in the lamination assessment were analyzed. Finally the applicability of ACU to *in situ* flaw monitoring was demonstrated by using multiple measurements of the same sample (with and without defects) and a multiparameter difference imaging method.

Materials and methods

Figure 1 illustrates the ACU NTM configuration. Two ACU transducers, transmitter and receiver, are aligned on both sides of the sample and are scanned together as a fixed unit in the X (beam length) and Y (beam width) directions. The insonification axis Z is perpendicular to the surfaces of the sample. For each scanned position the transmitter is excited with a burst signal and the waveform that is sensed at the receiver is then digitized. The recorded data is evaluated to obtain an image of faulty regions.

Sample preparation

ACU inspection was performed for a pallet of 66 glulam beams made of common spruce (*Picea abies* Karst.). Table 1 summarizes sample and defect geometries. The manufacture of sample groups A and B has been detailed elsewhere (Sanabria et al. 2010b,c). Samples of groups C and D are commercial glulam beams (Schilliger Holz AG, Haltiken, Switzerland) bonded with polyurethane resin in conformity with (EN 14080 2005) for a strength class GL24h. Type C consists each of two such beams glued in our laboratory room at room temperature with 250 g m^{-2} of PUR adhesive (HB 181, Purbond AG, Sempach Station, Switzerland) and pressed together with F-clamps, leaving artificially introduced non-glued areas. Samples of type D were used for flaw monitoring and were inspected before and after introducing 3 mm thick saw cuts. All samples were conditioned to normalized climatic conditions (T = 20°C, RH = 65%) until equilibrium moisture content (EMC) of 12% was reached and then they were measured at room temperature.

Theoretical considerations

The ACU NTM inspection of glulam was modeled as a $2L+1$ layer problem (L timber lamellas, L-1 glue lines, 2 air gaps) based on plane wave theory in aelotropic crystals (Musgrave 2003) and a LRT orthotropic model of wood elasticity (Bucur 2006). Figure 2a exemplifies the case $L = 1$. Assuming homogeneous anisotropy

Table 1 Glulam sample definition and ACU inspection settings. l, w, h, t, glulam beam length, width, height, thickness per lamella; Tx V, transmitted voltage; TS/SR, distance transmitter-sample/sample-receiver; Freq, peak frequency; Rx G, total reception gain; SNR, signal-to-noise ratio; TL, transmission losses.

Glulam sample definition			ACU experiment settings					
Group #	l, w, h, t (mm)	No. of lamellas, thickness of lamellas; description	TS, SR (mm)	Tx V (Vpp)	Freq[c] (kHz)	Rx G (dB)	SNR[d] (dB)	TL[e] (dB)
A (46)[a]	500, 100, 10, 5	2 lamellas; 5 mm	210, 80	115	4G 120	52	60	53
B (13)[a]	250, 170, 65, 32.5	2 lamellas; 32.5 mm	210, 55	100	1G 120	56	35	65
C (4)[a]	500, 160, 280, 40	2 commercial glulam beams (3 and 4 lamellas) glued together	80, 80	610	2S 120	70	15 (30)	110
D (3)[b]	280, 200, 280, 40	Commercial glulam beam; 7 lamellas	70, 70	614	2S 120	70	20 (40)	115

[a]Glued together with artificially introduced non-glued areas.
[b]Measured before and after introduction of saw cut defect.
[c]4G 120: n=4 Gaussian cycles f_o=120 kHz, $g(t)=\cos[2\pi f_o(t\text{-}n/2f_o)]\exp[\text{-}4.6(2tf_o/n\text{-}1)^2]$ $0\le t\le n/f_o$. 2S 120: n=2 Sinusoidal cycles f_o=120 kHz, $s(t)=\sin[2\pi f_o(t\text{-}n/2f_o)]$ $0\le t\le n/f_o$.
[d]Signal-to-noise ratio of recorded data through defect-free glulam. In brackets: SNR after in-band noise reduction (spatial averaging).
[e]TL is measured as the mean amplitude ratio between direct air signal and signal through defect-free glulam.

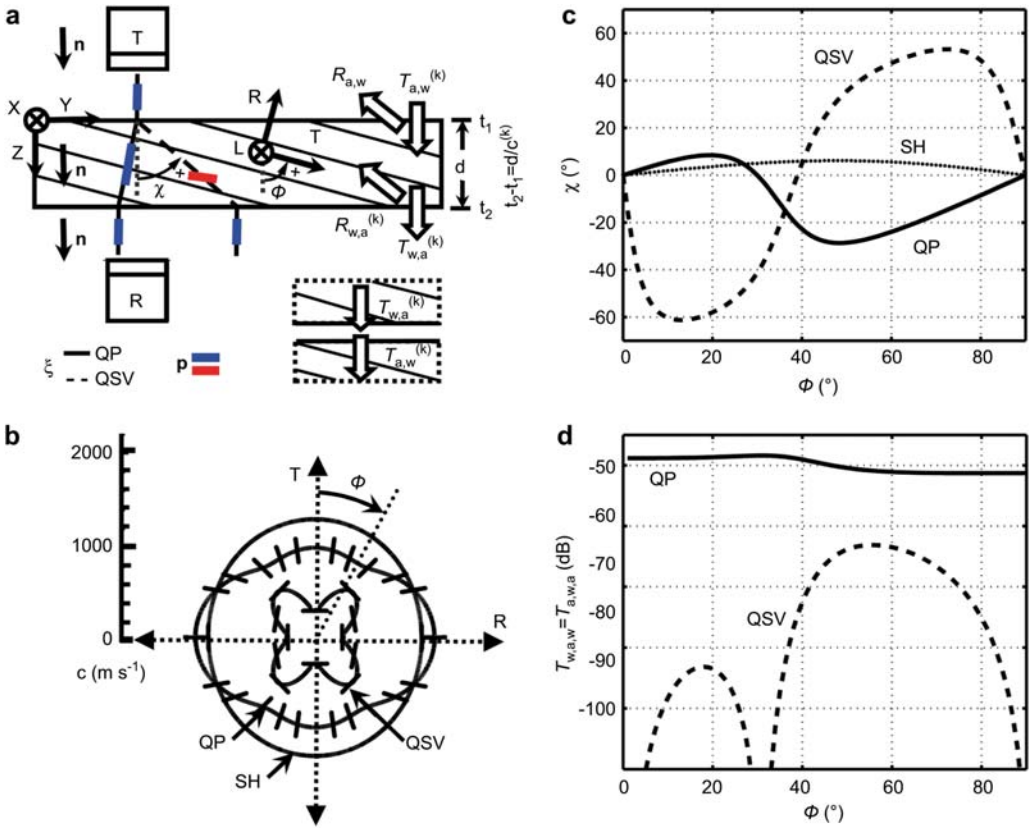

Figure 2 ACU NTM wave propagation model. a) Wave parameters and coordinate systems for a single timber lamella and a delaminated interface. b) Phase velocity surface and mode definition. c) Energy flux shifts as a function of the ring angle. d) Three layer transmission coefficients, the SH mode is not coupled.

along the wave path within a single layer and negligible grain distortion, the wave normal $\mathbf{n}=(0\ 0\ 1)^T$ is parallel to Z and plane wavefronts are perpendicular to the RT plane. Phase velocities c and polarization vectors $\mathbf{p}$ were calculated by vector transformation between XYZ ($\mathbf{n}$, $\mathbf{p}$) and LRT ($\mathbf{n}'$, $\mathbf{p}'$) as a function of the ring angle ϕ and performing eigen decomposition of the Christoffel tensor Γ_{ik}:

$$\sum_{k=1}^{3}(\Gamma_{ik}-\rho c^2\partial_{ik})p'_k=0 \quad \Gamma_{ik}=\sum_{j=1}^{3}\sum_{l=1}^{3}C_{ijkl}\,n'_j\,n'_l$$
$$i=1\ldots3 \qquad \mathbf{n}'=\mathbf{A}^{\mathbf{T}}\mathbf{n} \qquad \mathbf{p}=\mathbf{A}\mathbf{p}'$$
$$\mathbf{A}=\begin{bmatrix}1 & 0 & 0\\ 0 & \cos\phi & \sin\phi\\ 0 & -\sin\phi & \cos\phi\end{bmatrix} \tag{1}$$

where C_{ijkl} is the LRT stiffness tensor, ρ the density and ∂_{ik} the Kronecker delta. Figure 2b shows polar plots of c and $\mathbf{p}$ computed with spruce data according to (Hörig 1935): $C_{LLLL}=16.60$ GPa, $C_{RRRR}=0.79$ GPa, $C_{TTTT}=0.45$ GPa, $C_{LLRR}=0.44$ GPa, $C_{LLTT}=0.32$ GPa, $C_{RRTT}=0.20$ GPa, $C_{LRLR}=0.63$ GPa, $C_{LTLT}=0.78$ GPa, $C_{RTRT}=0.04$ GPa, $\rho=494$ kg m^{-3}. Three modes are defined by maximizing the dot product of $\mathbf{p}$ with XYZ, namely QP (quasi-longitudinal), QSV (quasi transverse, in-plane) and SH (purely transverse, out of plane). The SH mode is faster (1130–1260 ms^{-1}) than the QP mode (910–1270 ms^{-1}) except in the vicinity of R, the QSV mode is slower (280–620 ms^{-1}) than the other two. At R and T pure P and SV modes are coupled. Due to the non-sphericity of the velocity surface the energy flux $\boldsymbol{\xi}$ deviates from $\mathbf{n}$ except for R and T giving rise to a lateral shift χ (°):

$$\chi=\angle(\mathbf{n},\boldsymbol{\xi}) \quad \xi'_i\propto\sum_{j=1}^{3}\sum_{k=1}^{3}\sum_{l=1}^{3}C_{ijkl}\,p'_j\,p'_k\,n'_l \quad \xi=\mathbf{A}\boldsymbol{\xi}' \tag{2}$$

The ACU sound field coupled into glulam diverges from the insonification axis Z and propagates along $\boldsymbol{\xi}$, being only partially captured by the NTM receiver, large χ result in strong energy losses (Figure 2a). The energy flux shifts are highly dependent on the coupled mode and the orientation of the annual rings. Figure 2c is a plot of χ as a function of ϕ. The SH mode shows χ smaller than 6°, which explains that contact shear transducers polarized in the fiber direction perform best for glulam inspection (Dill-Langer et al. 2005a). The QP mode tends to align with T and R with an equilibrium point at $\phi=30°$ (pure P mode) and a 30° shift towards R at $\phi=50°$, deviations from T introduce smaller χ ($<10°$). The QSV mode typically shows largest χ (up to 60°) with a sign opposite to QP. A wave surface cusp at $\phi=39°$ aligns $\mathbf{n}$ and $\boldsymbol{\xi}$.

At delaminated interfaces a reduction of transmitted ultrasound energy is expected, due to the high acoustic impedance mismatch between solids and air. The amplitude contrast $L_{glued/non\text{-}glued}^{(k)}$ (dB) for a single echo of mode k is approximated by a three layer transmission coefficient $T_{w,a,w}^{(k)}$:

$$L_{glued/non\text{-}glued}^{(k)} = 20\log_{10}\frac{V_{glued}}{V_{non\text{-}glued}} \approx -20\log_{10} T_{w,a,w}^{(k)} = -20\log_{10}\left[T_{w,a}^{(k)} T_{a,w}^{(k)}\right]$$

$$\begin{cases} -R_{a,w} + \sum_{i=1}^{3} T_{a,w}^{(i)} p_3^{(i)} = 1 \\ R_{a,w} z_a n_j + \sum_{i=1}^{3} T_{a,w}^{(i)} z_w^{(i)} p_j^{(i)} = z_a n_j \end{cases} \qquad \begin{cases} -\sum_{i=1}^{3} R_{w,a}^{(i)} p_3^{(i)} + T_{w,a}^{(k)} = p_3^{(k)} \\ \sum_{i=1}^{3} R_{w,a}^{(i)} z_w^{(i)} p_j^{(i)} + T_{w,a}^{(k)} z_a n_j = z_w^{(k)} p_j^{(k)} \end{cases}$$

$$j = 1 \ldots 3 \qquad z_w^{(k)} = \rho c^{(k)} \qquad \mathbf{n} = \begin{pmatrix} 0 & 0 & 1 \end{pmatrix}^T \tag{3}$$

V_{glued} and $V_{non\text{-}glued}$ (V) are amplitude levels received through glued and non-glued timber. $T_{w,a,w}^{(k)}$ equals the coupling losses $T_{a,w,a}^{(k)}$ for the single lamella setup of Figure 2a and is the product of the two layer transmission coefficients $T_{w,a}^{(k)}$ and $T_{w,a}^{(k)}$, which result from traction and normal displacement continuity at air/wood interfaces and are functions of ρ, c and $\mathbf{p}$. $z_a = 427$ Pa s m^{-1} (Deutsch et al. 1997) and $z_w^{(k)}$ are acoustic impedances in air and wood; $R_{a,w}^{(k)}$ and $R_{w,a}^{(k)}$ are two-layer reflection coefficients. Figure 2d shows $T_{w,a,w}^{(k)}$ for each mode. The QP mode shows the best $\mathbf{p}$ match with P waves in air, with $T_{w,a,w} = 50 \pm 1.5$ dB. The QSV mode is coupled with $T_{w,a,w}$ at least 12 dB smaller than QP ($\phi = 56°$) and cancels for $\mathbf{p} \perp \mathbf{n}$, namely when pure SV modes occur ($\phi = 0°$, $\phi = 30°$, $\phi = 90°$). Accordingly, the SH mode is theoretically not coupled with the ACU NTM setup for any ϕ.

The generalization to L-layered glulam results in 2^{2L-1} propagation paths (Figure 3). The fastest path is named QPx and is followed by interfering QP/QSV modes. Secondary wave reflections between timber lamellas can be neglected at 120 kHz due to the 2.4 dB cm^{-1} attenuation coefficient in wood (estimated from the total transmission losses of Table 1). ϕ was extracted for each lamella and insonification position by using optical scans of the cross-section of the glulam beams.

Experimental setup

Table 1 summarizes the experimental settings for each sample group. The transducers are 120 kHz broadband planar Gas Matrix Piezoelectric Composites (NCG100-D50, The Ultran Group Inc., State College, PA, USA) with an active diameter of 50 mm. The air separation between transducers and sample was chosen to filter undesired wave reflections and to improve the lateral resolution. The samples were scanned with a 3 axes computed-controlled mechanical scanner synchronized with an arbitrary waveform generator and a data acquisition board. The system is detailed in (Sanabria et al. 2010b) together with the transmission and receiver electronics for sample groups A and B. Samples C and D were assessed with a second system developed for thick glulam inspection. A computer-generated pulsed excitation is driven into a High Power Tone Burst Pulser (RPR4000, RITEC Inc., Warwick, RI, USA) and the gated amplified output (up to 2 kVpp with 1% duty cycle) is fed to the transmitter transducer. A self-developed high-power resistive attenuator box was used at the output of the pulser for stabilization, broadband electric impedance matching and monitoring. Specific electronics were developed to synchronize the gated amplifier with the external excitation signal. The reception chain has an input referred noise of 0.9 nVrms Hz$^{-0.5}$ and consists of a low-noise preamplifier (5660C, Olympus NDT Inc., Waltham, MA, USA) and a broadband receiver (RPR4000). The transmission limits are given by the antenna noise of the ACU receiver transducer (5 nVrms Hz$^{-0.5}$, measured) and the maximum voltage that can be driven into the transmitter without damage (>1000 Vpp, manufacturer data). The signal-to-noise ratio (SNR) was measured as the nominal peak voltage received for defect-free timber divided by the rms noise value at a time gate prior to the fastest ACU wave. For 280 mm thick glulam we bridged 115 dB transmission losses with a SNR of 30 to 40 dB. Therefore, the assessment of thicker glulam is promising.

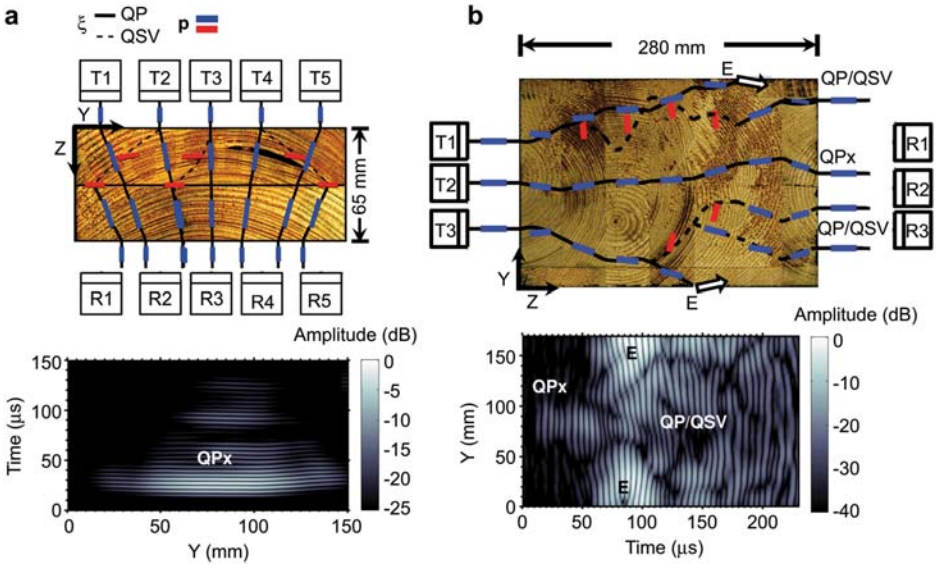

Figure 3 Wave propagation paths in defect-free glulam for a sample of type B (a) and a sample of type D (b). Top: path trajectories and polarization vectors. Bottom: average B-scans along Y-axis.

Data evaluation

The ACU NTM measurement data was stored in 3D datasets $V(x_i, y_j, t_n)$ (V) consisting of digitized time t_n waveforms for each scanned pixel (x_i, y_j), where i, j, n are discretization indexes. Spatial redundancy was achieved by using smaller scan steps (1 to 10 mm) than the outgoing 6 dB sound field diameter (30 mm for samples of type B). In-band noise reduction was implemented by computing for each scanned pixel an overlapped average of $L \cdot M$ spatially adjacent waveforms:

$$W(x_i, y_j, t_n) = \frac{1}{LM} \sum_{l=-(L-1)/2}^{(L-1)/2} \sum_{m=-(M-1)/2}^{(M-1)/2} V(x_{i+l}, y_{j+m}, t_n) \tag{4}$$

A 15×15 mm^2 averaging window (45 pixels) introduced a 16 dB SNR improvement, in good agreement with the theoretical $\sigma^2/(LM)$ variance reduction for averages of uncorrelated Gaussian sequences (17 dB). Next, the 3D dataset was reduced to a 2D ultrasonic image using two different strategies. The non-tracked approach computes the peak or rms amplitude for a fixed time window $[n_o, n_o+N]$:

$$A^{RMS}(x_i, y_j) = \sqrt{\frac{1}{N+1} \sum_{n=n_o}^{n_o+N} V(x_i, y_j, t_n)^2}$$
$$A^{PEAK}(x_i, y_j) = \max_{n \in [n_o,\ n_o+N]} V(x_i, y_j, t_n) \tag{5}$$

This method provides a global energy estimate for time intervals with interfering QP/QSV modes. The tracked approach exploits the continuity of spatially adjacent waveforms to calculate the amplitude of the QPx mode. A moving time window G of N samples length is actualized in each algorithm step k to be centered at the peak amplitude time position n_c measured in the previous iteration step:

$$n_c{}^0 = n_o \qquad x_i{}^0 = x_{i_o} \qquad y_j{}^0 = y_{j_o}$$
$$I: \quad A^{TRK}\left(x_i{}^k, y_j{}^k\right) = \max_{n \in \mathbf{G}^k} V\left(x_i{}^k, y_j{}^k, t_n\right)$$
$$II: \quad n_c{}^{k+1} = \arg\max_{n \in \mathbf{G}^k} V\left(x_i{}^k, y_j{}^k, t_n\right)$$
$$III: \quad \mathbf{G}^{k+1} = \left[n_c{}^{k+1} - N/2, n_c{}^{k+1} + N/2\right]$$
$$IV: \quad \left(x_i{}^k, y_j{}^k\right) = \{(x_{i_o}, y_{j_o}), (x_{i_o+1}, y_{j_o}), \ldots, (x_I, y_{j_o}), (x_{i_o-1}, y_{j_o}), \ldots, (x_1, y_{j_o}), (x_{i_o}, y_{j_o+1}), \ldots, (x_1, y_J), (x_{i_o}, y_{j_o-1}), \ldots, (x_1, y_1)\} \tag{6}$$

The algorithm starts the computation at a large amplitude region and explores a sequence of adjacent pixels (Eq. 6, IV) until A^{TRK} is completed, with $i=1\ldots I$ and $j=1\ldots J$. Typically a single wave cycle is tracked. The images are normalized to the maximum amplitude either in linear (a.u.) or in dB scale.

Difference imaging

Two measurements $V_1(x_i, y_j, t_n)$ and $V_2(x_i, y_j, t_n)$ of the same beam obtained at different times were compared and large differences were associated to in-service fault development. The amplitude difference estimator A^d is defined as a non-tracked rms ratio:

$$A^d(x_i, y_j) = \sqrt{\frac{\sum_{n=n_o}^{n_o+N} V_2(x_i, y_j, t_n)^2}{\sum_{m=n_o}^{n_o+N} V_1(x_i, y_j, t_m)^2}} \tag{7}$$

Amplitude-independent estimators were obtained from the correlation coefficient r defined as the correlation between waveforms normalized with the geometric mean of energies:

$$r\left(x_i, y_j, \tau_m\right) = \frac{\sum_n V_1\left(x_i, y_j, t_{n+m}\right) V_2\left(x_i, y_j, t_n\right)}{\sqrt{\sum_l V_1\left(x_i, y_j, t_l\right)^2 \sum_p V_2\left(x_i, y_j, t_p\right)^2}}$$
$$S^d\left(x_i, y_j\right) = \max_{m \in [n_o - N/2,\ n_o + N/2]} r\left(x_i, y_j, \tau_m\right)$$
$$\tau^d\left(x_i, y_j\right) = \tau_{m^d\left(x_i, y_j\right)}$$
$$m^d\left(x_i, y_j\right) = -n_o + \arg\max_{m \in [n_o - N/2,\ n_o + N/2]} r\left(x_i, y_j, \tau_m\right) \tag{8}$$

The domain of r is [-1, 1], with $r(x_i, y_j, \tau_m) = 1$ for two waveforms of the same shape and delayed by τ_m with respect to each other. Time τ^d and shape S^d difference estimators were defined as the peak position and value of r, respectively. Best results were obtained by evaluating a limited time window (40 μs) around the mean time delay n_o observed between the two datasets. Multiparameter difference imaging was performed combining binarized images from A^d, S^d and τ^d. An optimum probabilistic single-threshold STMAP binarization algorithm has been described by Sanabria et al. (2010a). The combination logic of Table 2 performed well for lamination defect inspection. In accordance with the theory, A^d is the most sensitive estimator.

Results and discussion

Wave propagation paths in glulam

Figure 3a shows computed propagation paths and measured B-scans for a defect-free sample of group B. The energy flux

Table 2 Truth table for multiparameter difference imaging.

$A^d(x_i, y_j)$	$S^d(x_i, y_j)$	$\tau^d(x_i, y_j)$	Multi-parameter
G	G	G	G
G	G	D	G
G	D	G	G
G	D	D	U
D	G	G	U
D	G	D	D
D	D	G	D
D	D	D	D

G, glued material; D, defect material; U, unknown state.

ξ of the QPx mode (QP/P/QP) tends to align with the material axis R and is only parallel to Z for transmission at the center of the beam width T3, deviating up to 25 mm for T1 and T5. As a consequence, the amount of energy captured at R1 and R5 is systematically 15 dB below the amplitude at R3. The most efficient QP/QSV path (QSV/SV/QP) is typically 20 dB below the QPx mode, due to the larger energy flux shifts and coupling losses and could not be reliably assessed in the B-scans.

Figure 3b represents typical wave paths in defect-free samples of groups C and D, a 15 layer model (seven timber lamellas, six glue lines, two air gaps) results in 8192 possible propagation paths. The QPx mode was only captured with the NTM setup at the center of the beam width R2, where the alignment between Z and R tends to be best. At R1 and R3 several QP/QSV paths, with small total ξ shifts, were received more efficiently than the QPx mode, with a time separation of at least 80 μs from the latter. They interfere in a complex pattern leading to ultrasound signal accumulation in a large time interval (>200 μs). For some of the inspected beams, additional energy accumulation (E) in the vicinity of the Y edges of the sample was qualitatively interpreted as low grazing beam reflections at the lateral surfaces of the sample. The modeling of the propagation of a finite sound field through heterogeneous anisotropic lamellas taking into account lateral edge effects is the subject of a separate work (Sanabria et al. 2010d).

Imaging of bonding defects with single measurement

Figure 4 demonstrates successful imaging of an 80×80 mm^2 non-glued region (dashed square) limited by a 580 μm thick and 10 mm wide aluminum frame in a sample of type B. Direct air paths (A) are filtered out in time (Figure 4a) since the sound speed in air is lower (346 ms^{-1}) than in spruce (W). Figure 4b was obtained with non-tracked imaging. The diffraction of ultrasound energy around the defect distorts its geometry and reduces $L_{glued/non\text{-}glued}$ to <15 dB (Figure 4e). Tracking the first incoming oscillation (Figure 4c) improves the imaging, $L_{glued/non\text{-}glued}$ being only limited by the noise floor of the system (35 dB, Table 1) and the lateral resolution of the sound field (20 dB amplitude reduction at 20 mm from glued/non-glued transition). The ξ shifts introduce systematic amplitude variations along Y for defect-free regions (Figure 3a), which were partially compensated for by normalizing the images with a calibration amplitude profile (Figure 4d). Numerical simulations of the interference effects in the glue line have shown that $L_{glued/non\text{-}glued}$ is reduced from 50 to 20 dB for a delamination gap of 10 μm, adhesive penetration in defect regions and non-adherent dry glue regions have also been assessed with this method (Sanabria et al. 2010c).

Figure 5 shows ACU NTM inspection of a sample of group C with a non-glued region at the third lamination from

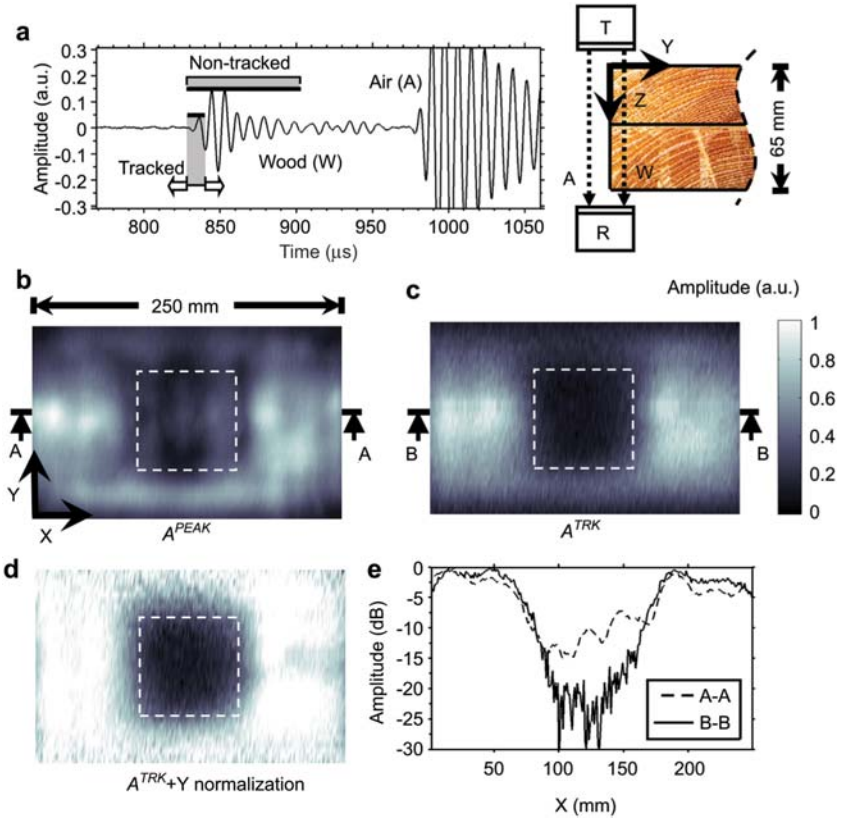

Figure 4 ACU NTM imaging of bonding defects in samples of type B. a) Typical waveform received for defect-free glulam at the sample edge and time windows used for amplitude imaging. b) and c) were computed with non-tracked and tracked approaches, respectively. d) was obtained from c) after heterogeneity compensation in Y-axis. e) Amplitude contrast at defect region.

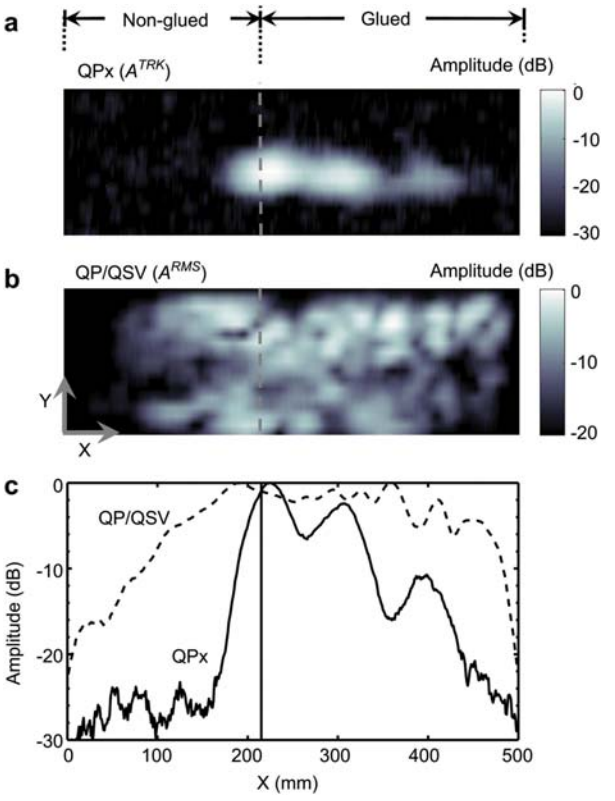

Figure 5 ACU NTM imaging of bonding defects in samples of type C. a) Tracked amplitude imaging of the first oscillation of the QPx mode. b) Non-tracked amplitude imaging of the first 50 μs of the QP/QSV modes. c) Amplitude contrast at defect region.

X = 0 to 215 mm. Figure 5a was computed by tracking the QPx mode, the assessment was limited in Y to the center of the beam width, where the ξ shifts are sufficiently small to allow for NTM reception (Figure 3b). Figure 5b is a non-tracked rms image of the first 50 μs of the QP/QSV modes. Ultrasonic energy is received for all Y positions; however, the effective lateral resolution is reduced due to the uncertainty region defined by the ξ shifts of all paths that interfere at the receiver (Figure 3b). Figure 5c compares amplitude profiles of both images, the QPx mode is reduced by 20 dB at 40 mm from the transition between glued and non-glued areas, down to the noise floor of the system; the QP/QSV modes show the same contrast only at 210 mm from the transition. Large amplitude variability is observed in both Y and X, the latter of which can be associated to energy flux shifts in the fiber direction due to an accumulation of grain distortions, e.g., at knot positions. The imaging is therefore limited to large defect areas ($>100\times100$ mm^2).

Defect monitoring with difference imaging

The reproducibility error of ACU NTM measurements of samples of type A repeated after one year was lower than 1.5% (Sanabria et al. 2010b). Flaw monitoring was demonstrated by comparing two ACU NTM measurements (with a one-day interval) of samples of type C, obtained before and after introducing saw cut defects. A 100 μs time gate containing both QPx and QP/QSV modes was evaluated. Figures 6a and b show A^{RMS} imaging for the two measurements, a reproducible amplitude variability pattern is observed in defect-free regions for both images, which partially masks the amplitude decrease in the defect region of Figure 6b. These variations are associated to the heterogeneous structure of glulam, and are significantly reduced by means of difference imaging with A^d, therefore highlighting the geometry of the saw cut (Figure 6c). The performance of the difference method is limited by the dynamic range of the electronics; signals below the noise floor cannot be compared.

Figure 6d shows typical snapshots of the correlation coefficient r. At glued positions (G) the envelope of r decreases monotonically from the τ origin, thus indicating a high similarity between compared waveforms. However, at defect positions (D) r shows a multimodal pattern, which assesses changes in the interference of wave propagation paths at the ACU receiver. These amplitude-independent variations are summarized in time τ^d (Figure 6e) and shape S^d (Figure 6f) difference images.

Figure 7 shows optimally binarized ACU images for three saw cut geometries. Figure 7b was obtained from a single measurement with A^{RMS}. This approach introduces false hits in some cases (1) and is too conservative in others (2). A clear improvement was observed with A^d (Figure 7c), which satisfactorily assesses the position and geometry of the defects. The most robust estimator was achieved with multiparameter difference imaging according to Table 2 (Figure 7d), with most of the remaining false hits (3) being classified as unknown states. Failures to detect defect regions were, in several cases, associated with large knots that were visually assessed at the external surfaces of the sample (4). The fiber distortion around the knot may deviate the wave paths around the defect area. Similar effects can explain the displacement of an imaged defect region (5) from its actual position. The effect of varying moisture content (MC) in difference imaging is not yet clarified. According to 140 kHz results of Vun et al. (2008), at T = 23°C a MC change from 27 to 151% introduces ACU NTM transmission variations of 6 dB in 25 mm thick solid wood. Sakai et al. (1990) measured at 1 MHz for several wood species transmission variations below 2 dB and sound speed variations of 10% for a MC interval between 0% and 20%. Sandoz (1993) observed at 50 kHz similar sound speed variations in structural wood grading.

Reduction of impact of wood heterogeneity and anisotropy

Based on Table 3 the amplitude variability is compared for specific imaging algorithms and sample groups A to D, defined as the ratio between the 95% and 5% percentiles, Q_P, in a 125 mm^2 defect-free region $i\in[i_1, i_2]$, $j\in[j_1, j_2]$. The total 2D variability Δ^{XY} (dB) was split into 1D heterogeneity components Δ^X and Δ^Y in X and Y corresponding to the mean variability along (L) and across (RT) the fiber direction, respectively:

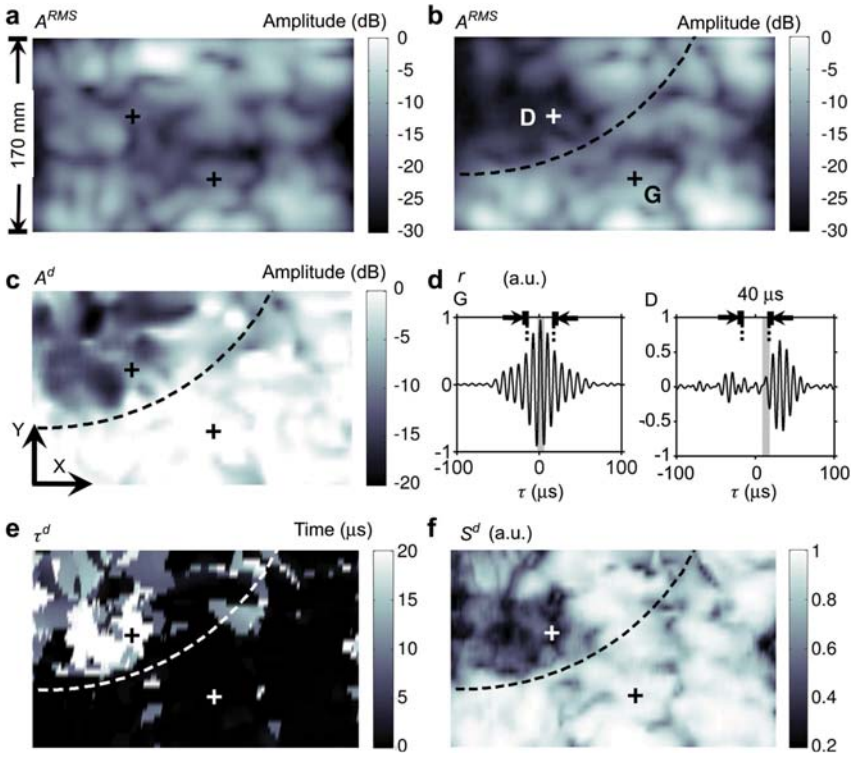

Figure 6 ACU NTM difference imaging of saw cut defects in a sample of type D corresponding to Figure 7, center. a) and b) are non-tracked amplitude images before and after introducing the saw cut defect, respectively, for a 100 µs gate containing QPx and QP/QSV modes. c) was obtained with difference amplitude imaging. d) shows snapshots of the correlation coefficient for glued (G) and defect (D) material. Time e) and shape estimators f) were computed from a 40 µs time gate.

$$\Delta^{XY} = 20\log_{10}\frac{Q_{.95}\left[A(x_i,y_j)\right]_{i\in\mathbf{I},\,j\in\mathbf{J}}}{Q_{.05}\left[A(x_i,y_j)\right]_{i\in\mathbf{I},\,j\in\mathbf{J}}} \qquad \mathbf{I}=[i_1,i_2] \qquad \mathbf{J}=[j_1,j_2]$$

$$\Delta^{X} = \frac{1}{j_2\text{-}j_1+1}\sum_{j=j_1}^{j_2} 20\log_{10}\frac{Q_{.95}\left[A(x_i,y_j)\right]_{i\in\mathbf{I}}}{Q_{.05}\left[A(x_i,y_j)\right]_{i\in\mathbf{I}}} \qquad \Delta^{Y} = \frac{1}{i_2\text{-}i_1+1}\sum_{i=i_1}^{i_2} 20\log_{10}\frac{Q_{.95}\left[A(x_i,y_j)\right]_{j\in\mathbf{J}}}{Q_{.05}\left[A(x_i,y_j)\right]_{j\in\mathbf{J}}} \tag{9}$$

Δ^{XY} grows with the thickness of the glulam beam, the variability in sample group B is 10 dB larger than in A. Most of this heterogeneity could be associated to variations of captured energy with the NTM setup due to changes in ξ. Particularly, Δ^Y was for all sample groups twice as large as Δ^X, owing to the dependency of the RT shifts with ϕ (Figure 2c). For samples of type A, a theoretical 1.5 dB variation was computed for $\phi = 45°$ to 90° in agreement with the Δ^Y values observed. Δ^{XY} is largest for non-tracked images, since large time gates integrate multiple wave reflections between the 5 mm thick timber lamellas. This effect does not occur in samples of type B, which show similar Δ^{XY} values for tracked and non-tracked imaging. However, the tracked approach is less influenced by energy diffraction at sample edges or around defects, giving a systematic variability pattern in Y (Figure 4c), which can be reduced by 6 dB down to Δ^X (4 dB) by means of Y normalization. Samples groups C and D show only 4 dB larger Δ^{XY} than group B. The integration of a large number of interfering QPx/QSV paths and the spread of the sound field homogenize the energy received at the glulam beam output. The difference imaging technique eliminates repeatable variability patterns along X and Y and improves Δ^{XY} by 10 dB.

Conclusion

A novel normal transmission air-coupled ultrasound imaging system was successfully applied to detect bonding and saw cut defects in multilayered glulam beams up to 280 mm in height. For defect-free material, 115 dB transmission losses (coupling, material attenuation) were bridged by exciting off-the-shelf 120 kHz piezoelectric transducers with a 600 Vpp pulsed excitation and by means of reception electronics with an input referred noise of 0.9 nVrms $Hz^{-0.5}$. The ultrasonic waveforms received through defect regions are additionally attenuated by up to 50 dB; in practice, the amplitude contrast is limited by the SNR of defect-free signals (30 to 40 dB).

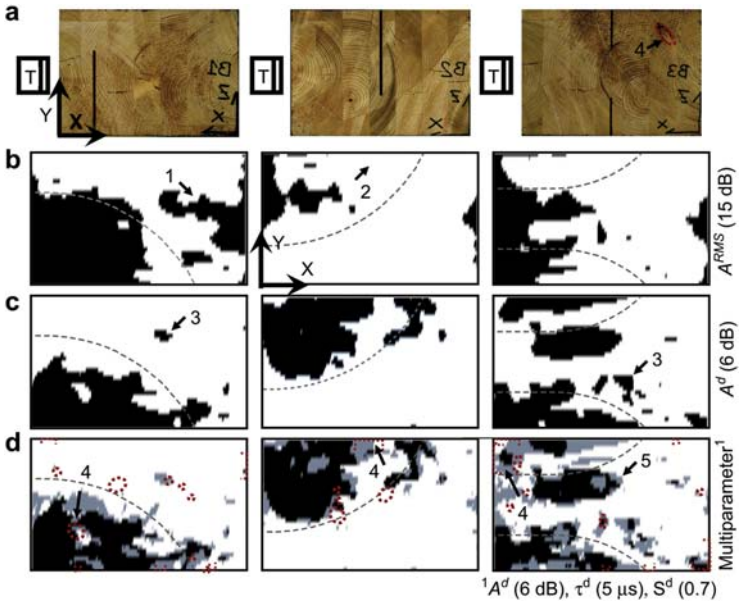

Figure 7 ACU NTM segmentation of saw cut defects in samples of type D, the estimators of Figure 6 were binarized with the thresholds indicated in brackets. a) Optical scans of the beam cross-sections and defect position with respect to transmitter T. b) Binarized non-tracked images, (1) and (2) are false negatives and false positives, respectively. c) Binarized difference images, (3) are residual false negatives. d) Multiparameter difference imaging according to Table 2, (4) indicates knot positions assessed optically from the sample surfaces, the defect region (5) is displaced from its actual position.

The glulam beams were modeled as anisotropic composites. QP and QSV modes are coupled in each lamella. They are deviated from the insonification axis as a function of the ring angle by up to 30° and 60°, respectively, introducing 15 dB variability in the energy captured by the receiver transducer. The fastest QPx mode was efficiently detected only at the center of the beam width and it was followed in time by interfering QP/QSV modes, which were received at all width positions. The QP/QSV paths were detected with lowest lateral resolution, due to the accumulation of the energy flux shifts of all interfering modes; defect free regions of 100×100 mm^2 could be detected.

The imaging was improved by spatial processing based on the low reproducibility error (1.5%) and arbitrary scanning resolution of ACU. Overlapped averaging improved the SNR by 16 dB. Amplitude tracking captured only the first incoming oscillation thus reducing undesired diffraction around defect areas. A normalization procedure reduced the amplitude heterogeneity by 6 dB. Defect monitoring based on difference imaging reduced the variability by 10 dB, multiparameter segmentation accurately reproduced the defect geometry. The new method is non-invasive and therefore applicable not only to production lines but also to *in situ* inspection. In future work, the propagation phenomena will be investigated, which are associated to grain deviations and density and stiffness inhomogeneities (due to knots, earlywood/latewood structure or moisture gradients), together with alternative ACU insonification setups. The wave propagation equations will be perturbed to incorporate time-dependant heterogeneity, for instance spatially varying moisture profiles induced by the slow hygroscopic response of structural timber to in-service climatic variations (Gereke 2009; Angst and Malo 2010). The use of ACU together with multiparameter difference imaging and normalization procedures along the fiber direction have a high potential for heterogeneity compensation and defect classification.

Table 3 Mean amplitude variability in defect-free glulam. The total variability Δ^{XY} in a 125 mm^2 region is compared to the heterogeneities Δ^X and Δ^Y along (L) and across (RT) the fiber direction, respectively.

Group #	Amplitude estimator (no. samples)	L: Δ^X (dB)	RT: Δ^Y (dB)	Total: Δ^{XY} (dB)
A	A^{RMS} QPx (18)	1.2	2.1	2.3
	A^{PEAK} QPx (18)	0.9	1.7	1.8
	A^{TRK} QPx (18)	0.5	1.5	1.5
B	A^{RMS} QPx (13)	5	10	12
	A^{PEAK} QPx (13)	5	10	11
	A^{TRK} QPx (13)	4	10	11
	A^{TRK} QPx+Y norm. (13)	4	4	6
C/D	A^{TRK} QPx (4)	16	–	16
	A^{RMS} QP/QSV (7)	7	13	15
	A^{d} QP/QSV (3)	4.2	5	5.5

Acknowledgements

This research was supported by the Swiss National Science Foundation under contract 200021-115920. The authors acknowledge the work of Oliver Tolar, Livia Zumofen, Fabian Binkert, Danniel Gómes, Claudio Weiss and Dominik Mächler in the design of the mechanics and electronics of the ACU system, together with the acquisition and evaluation of experimental data. Thomas Schnider

and Christian Müller are also credited for their contribution in the manufacture of glued timber samples.

References

Algernon, D., Grafe, B., Mielentz, F., Köhler, B., Schubert, F. (2008) Imaging of the elastic wave propagation in concrete using scanning techniques: application for impact-echo and ultrasonic echo methods. J. Nondestruct. Eval. 27:83–97.

Angst, V., Malo, K.A. (2010) Moisture induced stresses perpendicular to the grain in glulam: review and evaluation of the relative importance of models and parameters. Holzforschung 64:609–617.

Benedetti, P. (2003) Method and device for testing the presence of defects in the production of plane boards. EP Patent 1324032A1.

Berglind, H., Dillenz, A. (2003) Detection of glue deficiency in laminated wood with pulse thermography. J. Wood Sci. 49:216–220.

Blomme, E., Bulcaen, D., Cool, T., Declercq, F., Lust, P. (2010) Air-coupled ultrasonic assessment of wood veneer. Ultrasonics 50:180–187.

Blum, R. (1997) Verfahren zur Erkennung von Spaltern in Span- und MDF-Platten und Vorrichtung zur Durchführung des Verfahrens. DE Patent 19519669C1.

Bucur, V. Acoustics of Wood. Springer, Berlin, 2006.

Bucur, V., ed. Delamination in Wood, Wood Products and Wood-Based Composites. Springer, Berlin, 2011.

Dahmen, S., Ketata, H., Hédi, M., Hosten, B. (2010) Elastic constants measurement of anisotropic Olivier wood plates using air-coupled transducers generated Lamb wave and ultrasonic bulk wave. Ultrasonics. 50:502–507.

Deutsch, V., Platte, M., Vogt, M., Verein Deutscher Ingenieure. Ultraschallprüfung: Grundlagen und industrielle Anwendungen. Springer, Berlin, 1997.

Dill-Langer, G. (2004) Schädigung von Brettschichtholz bei Zugbeanspruchung rechtwinklig zur Faserrichtung. Universität Stuttgart, Dissertation (PhD-Thesis).

Dill-Langer, G., Aicher, S., Bernauer, W. (2005a) Reflection measurements at timber glue-lines by means of ultrasound shear waves. Otto Graf J. 16:273–283.

Dill-Langer, G., Bernauer, W., Aicher, S. (2005b) Inspection of glue-lines of glued-laminated timber by means of ultrasonic testing. In: 14th International Symposium on Nondestructive Testing of Wood, Eberswalde, Germany, pp. 49–60.

Dimanche, M., Capretti, S., Del Senno, M., Facaoaru, I. (1994) Validation of theoretical approach for the detection of delamination in glued laminated beams. In: First European Symposium on Nondestructive Evaluation of Wood, Sopron, Hungary, pp. 250–260.

Dunky, M., Niemz, P. (2002) Holzwerkstoffe und Leime: Technologie und Einflussfaktoren. Springer, Berlin.

EN 391 (2001) Glued laminated timber – Delamination test of glue lines.

EN 14080 (2005) Timber structures – Glued laminated timber – Requirements.

Fagus GreCon Greten GmbH & Co. KG (1994) Device for monitoring the quality of laminar materials, preferably based on wood, such as chipboard or plywood, by means of an ultrasonic transmitter. DE Patent 3742844C2.

Follrich, J., Stöckel, F., Konnerth, J. (2010) Macro- and micromechanical characterization of wood-adhesive bonds exposed to alternating climate conditions. Holzforschung 64:705–711.

Gan, T.H., Hutchins, D.A., Green, R.J., Andrews, M.K., Harris, P.D. (2005) Noncontact, high-resolution ultrasonic imaging of wood samples using coded chirp waveforms. IEEE T Ultrason Ferr. 52:280–288.

Gereke, T. (2009) Moisture-induced stresses in cross-laminated wood panels. ETH Zurich, Dissertation (PhD-Thesis).

Gustafsson, P.J., Hoffmeyer, P., Valentin, G. (1998) DOL behaviour of end-notched beams. Holz Roh- Werkst. 56:307–317.

Hasenstab, A. (2006) Integritätsprüfung von Holz mit dem zerstörungsfreien Ultraschallechoverfahren. Technische Universität Berlin. Dissertation (PhD-Thesis).

Hörig, H. (1935) Anwendung der Elastizitätstheorie anisotroper Körper auf Messungen an Holz. Arch. Appl. Mech. 6:8–14.

Hsu, D.K., Utrata, D., Kuo, M. (2010) NDE of lumber and natural fiber based products with air coupled ultrasound. Rev. Quant. Nondestruct. Eval. 29:1533–1540.

Hu, L.J., Gagnon, S. (2007) X-ray based scanning technique for non-destructive evaluation of finger-joint strength. In: 15th International Symposium on NDT of Wood, Duluth, MN, USA.

Hyvärinen, V. (2007) Non-contact ultrasonic inspection of boards. In: 15th International Symposium on NDT of Wood, Duluth, Minnesota, USA.

Jönsson, J.H. (2004) Internal stresses in the cross-grain direction in glulam induced by climate variations. Holzforschung 58:154–159.

Jönsson, J.H. (2005) Internal stresses in glulam due to moisture gradients in the grain direction. Holzforschung 59:18–22.

Jönsson, J.H., Svensson, S. (2004) A contact free measurement method to determine internal stress states in glulam. Holzforschung 58:148–153.

Kägi, A., Niemz, P., Mandallaz, D. (2006) Influence of moisture content and selected technological parameters on the adhesion of one-part polyurethane adhesives under extreme climatical conditions. Holz Roh- Werkst. 64:261–268.

Kunkle, J., Vun, R.Y., Eischeild, T., Langron, M., Bhardwaj, N., Bhardwaj, M., The Ultran Group. (2006) Phenomenal advancements in transducers and piezoelectric composites for non-contact ultrasound and other applications. In: European Conference on Non-Destructive Testing (ECNDT), Berlin, Germany.

Maeva, E., Severina, I., Bondarenko, S., Chapman, G., O'Neill, B., Severin, F., Maev, R.G. (2004) Acoustical methods for the investigation of adhesively bonded structures: a review. Can. J. Phys. 82:981–1025.

Musgrave, M.J.P. Crystal acoustics. Holden-Day, San Francisco, 2003.

Niemz, P., Gereke, T. (2009) Effect of short and long-term humidity variations on the moisture content and properties of wood. Bauphysik 31:380–385.

Osterloh, K., Rädel, C., Zscherpel, U., Meinel, D., Ewert, U., Bücherl, T., Hasentab, A. (2008) Fast neutron radiography and tomography of wood. Insight. 50:307–311.

Sakai, H., Minamisawa, A., Takagi, K. (1990) Effect of moisture content on ultrasonic velocity and attenuation in woods. Ultrasonics 28:382–385.

Sanabria, S.J., Wyss, P., Neuenschwander, J., Niemz, P., Sennhauser, U. (2010a) Assessment of glued timber integrity by limited-angle microfocus X-ray computed tomography. Holz Roh-Werkst. doi: 10.1007/s00107-010-0509-8.

Sanabria, S.J., Müller, C., Neuenschwander, J., Niemz, P., Sennhauser, U. (2010b) Air-coupled ultrasound as an accurate and reproducible method for bonding assessment of glued timber. Wood Sci. Technol. doi: 10.1007/s00226-010-0357-z.

Sanabria, S.J., Neuenschwander, J., Niemz, P., Sennhauser, U. (2010c) Structural health monitoring of glued laminated timber with a novel air-coupled ultrasound method. In: 11th World Conference on Timber Engineering, Riva del Garda, Trentino, Italy.

Sanabria, S.J., Furrer, R., Neuenschwander, J., Niemz, P., Sennhauser, U. (2010d) Air-coupled ultrasound wave propagation in glued laminated timber structures applied to bonding quality assessment. In: 2010 IEEE International Ultrasonics Symposium, San Diego, CA, USA.

Sandoz, J.L. (1993) Moisture content and temperature effect on ultrasound timber grading. Wood Sci. Technol. 27:373–380.

Scheffler, M., Weber, T., Niemz, P., Hardtke, H.J. (2007) Determination of residual stress in bonded wood components. Holzforschung 61:285–290.

Schrödter, A., Niemz, P. (2006) Studies on the influence of temperature and timber moisture on the failure behaviour of selected adhesives under tensile shear load. Holztechnol. 47:24–32.

Stöessel, R. (2004) Air-Coupled Ultrasound Inspection as a New Non-Destructive Testing Tool for Quality Assurance. Universität Stuttgart, Dissertation (PhD-Thesis).

Vun, R.Y., Hoover, K., Janowiak, J., Bhardwaj, M. (2008) Calibration of non-contact ultrasound as an online sensor for wood characterization: effects of temperature, moisture, and scanning direction. Appl. Phys. A–Mater. Sci. Process. 90:191–196.

Received September 20, 2010. Accepted December 31, 2010.
Previously published online March 14, 2011.